THE ASTRONOMICAL JOURNAL, 117:1063–1076, 1999 February

MAPPING THE VARIEGATED SURFACE OF PLUTO

ELIOT F. YOUNG
Southwest Research Institute, Suite 426, 1050 Walnut Street, Boulder, CO 80302
KARLA GALDAMEZ
12001 Pomering Drive, Downey, CA 90240
MARC W. BUIE
Lowell Observatory, 1400 West Mars Hill Road, Flagstaff, AZ 86001
RICHARD P. BINZEL
Department of Earth, Atmospheric, and Planetary Sciences, Room 54-410, Massachusetts Institute of Technology, Cambridge, MA 02139
AND
DAVID J. THOLEN
Institute for Astronomy, University of Hawaii, 2680 Woodlawn Drive, Honolulu, HI 96822
Received 1998 May 14; accepted 1998 August 12

ABSTRACT

During the period from 1985 through 1990, Pluto and its satellite Charon underwent a series of transits, eclipses, and occultations, which are collectively called "mutual events." The albedo distribution of Pluto's sub-Charon hemisphere can be determined from these events with a spatial resolution that surpasses any current direct-imaging schemes. We use an iterative technique to determine a map of Pluto's sub-Charon hemisphere with resolutions down to 200 km in some areas. This map resolves a localized bright feature that may be due to condensation around a geyser or in a crater.

Key words: planets and satellites: individual (Pluto, Charon)

1. INTRODUCTION

Soon after Charon's discovery in 1978, it was realized that the plane of Charon's orbit was nearly parallel to the Pluto-Earth line of sight (Andersson 1978). Several observers kept watch for eclipses, since Charon was expected to pass in front of and behind Pluto given an orbit-plane axis that was perpendicular to the line of sight to Earth. The first recognized transit of Pluto by Charon was observed on 1985 February 17, by R. P. B. (Binzel et al. 1985). Since Pluto and Charon are locked into mutually synchronous orbits with a period of $\sim$6.4 days, there were opportunities to watch a transit (and/or an eclipse) of Pluto by Charon or an occultation of Charon by Pluto every $\sim$3.2 days. Except for a few gaps due to Earth's moving briefly out of the cone of Charon's shadow, the mutual-event season lasted 6 years (Binzel & Hubbard 1997).

An important application of the mutual events is to map Pluto's surface. Transits of Pluto typically lasted a few hours, during which time the flux received from the Pluto-Charon system dropped by as much as $\sim$40% before returning to its original baseline as Charon moved across Pluto's surface. Since Pluto and Charon always show each other the same face (i.e., they are locked in mutually synchronous orbits), only one face of Pluto was transited by Charon, as was just one face of Charon occulted by Pluto. Several groups have used the mutual events to derive the albedos of regions as they were covered and uncovered (see Buie, Young, & Binzel 1997b for a review). With enough transits, one can piece together a mosaic of Pluto's entire sub-Charon hemisphere. This paper combines 18 inferior events (Charon in front of Pluto) to produce an improved map of Pluto's sub-Charon hemisphere.

The map-making process is especially sensitive to noise, since it is the point-to-point differences in brightness that determine surface albedos, and these differences amplify the noise in the light curve. A conventional least-squares fit produces a map with negative albedos or pixels with albedos several times higher than 1, often right next to one another. We use a linear model to translate an estimate of Pluto's surface into a synthetic light curve, but instead of *inverting* the matrix that relates Pluto's albedo distribution to the observed light curves, we iteratively apply the *adjoint*, as suggested by Claerbout (1998), which is a much more robust process. Furthermore, we constrain the derivatives of the light curves as an alternative to smoothing them, with good results (i.e., the elimination of illegal pixel values while maintaining most of the spatial resolution).

Pluto's surface albedo distribution is dominated by the transport of volatiles, but the locations of bright and dark surface elements have not yet been explained by any simple insolation-driven model. In this paper, we combine two important mutual-event data sets for the first time, and we are able to map parts of Pluto with spatial resolutions approximately 5 times higher than previous efforts. As is usually the case, the higher resolutions yield new features and raise new questions.

2. THE DATA SETS

The maps in this paper are based on two sets of *B*-filter inferior light curves, summarized in Table 1. One set was obtained primarily by R. P. B. at the University of Texas McDonald Observatory, the other by D. J. T. and M. W. B. at the University of Hawaii 88 inch (2.2 m) telescope.

2.1. *Coverage by the Events*

As Pluto moves around the Sun, the plane of Charon's orbit appears to shift, so that first Pluto's northern hemisphere (in 1985 and 1986) and later its southern hemisphere (1989 and 1990) are covered by Charon and its shadow. Charon's shadow can cover a significant amount of Pluto, especially when the sub-Earth and subsolar points on Pluto are separated—generally early or late in the Pluto observing season. We assume that Pluto's radius is 1183 km and

TABLE 1

LIST OF EVENTS

DATE	FIRST CONTACT	SECOND CONTACT	MIDEVENT	THIRD CONTACT	FOURTH CONTACT	LATITUDE (deg)	
						Subsolar	Sub-Earth
D. J. T., M. W. B.:							
1985 Mar 21	6.51	...	7.53	...	8.54	−4.5	−5.7
1985 Dec 14	11.55	...	13.38	...	15.22	−3.1	−4.2
1986 Jan 15	10.06	...	12.01	...	13.56	−2.37	−3.97
1986 Mar 20	7.09	...	9.04	...	10.59	−2.35	−3.59
1986 Apr 21	5.55	...	7.41	...	9.26	−2.98	−3.41
1987 Mar 19	8.03	10.03	10.13	10.32	12.22	−0.16	−1.48
1988 Feb 14	10.52	...	12.49	...	15.16	2.14	0.41
1988 Apr 18	7.43	9.41	9.58	10.16	12.03	1.43	0.80
1988 May 7	11.34	13.25	13.57	14.15	16.04	0.97	0.92
1988 May 20.....	6.09	7.58	8.35	8.48	10.44	0.66	0.99
1988 Jun 8	10.01	11.51	12.32	12.37	14.41	0.23	1.11
1989 May 19.....	7.43	...	9.44	...	11.31	2.87	3.09
R. P. B.:							
1985 Feb 17	8.09	...	9.20	...	10.31	−4.24	−5.88
1986 Mar 20	7.09	...	9.04	...	10.59	−2.35	−3.59
1987 May 22.....	4.59	7.15	7.26	7.35	9.30	−1.53	−1.09
1988 Apr 18	7.43	9.41	9.58	10.16	12.03	1.43	0.80
1989 Apr 30	3.50	...	5.46	...	7.24	3.34	2.97
1990 Feb 24	9.11	...	9.45	...	10.51	6.41	4.69

Charon's is 620 km (Young & Binzel 1994). Note that our radii are larger than those used in Buie, Tholen, & Horne's (1992) mapping effort (radii of 1154 and 576 km for Pluto and Charon, respectively). We repeated the entire map construction process with the smaller radii, with no significant changes in the size or location of bright and dark features (shown in Fig. 7 below).

Both data sets include transits that collectively cover Pluto's entire sub-Charon hemisphere. Table 1 lists the events used in this paper, and Figure 1 shows a snapshot of each event.

2.2. *Putting the Light Curves on a Common Photometric Scale*

Each mutual event was observed when Pluto was at a particular distance and phase angle. All of the light curves must be reduced to a common geometry or else the maps of Pluto will have dark or bright "racing stripes" due to the

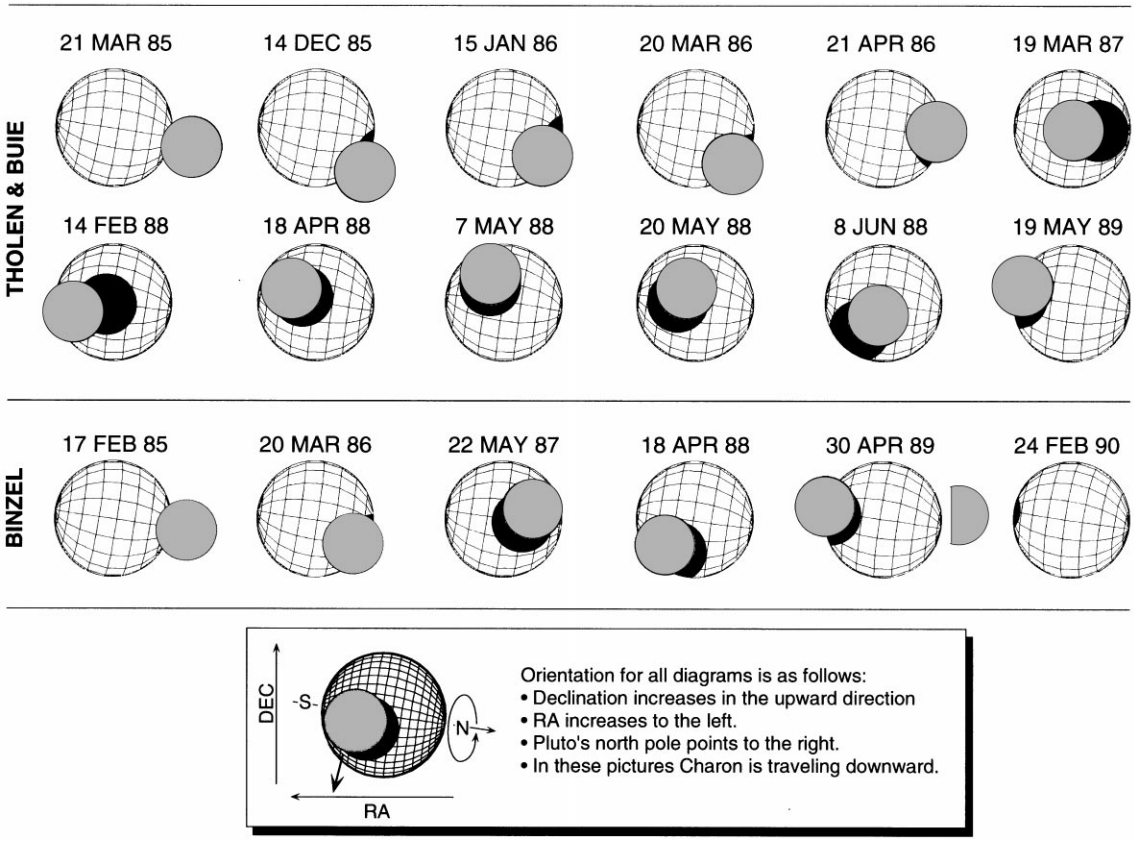

FIG. 1.—Diagrams of the 18 inferior events (Charon transiting in front of Pluto)

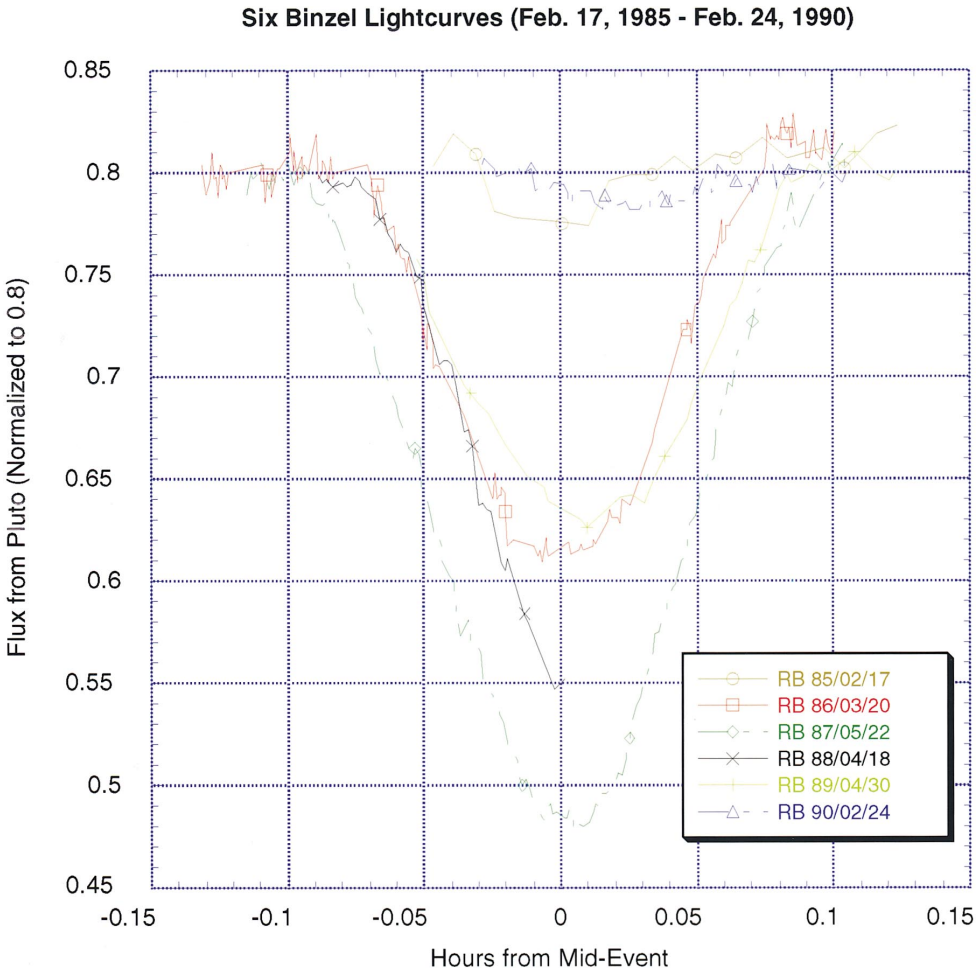

FIG. 2.—The 18 light curves, converted to fluxes with Charon's contribution removed

varying photometric scale among all the light curves. This section describes how we scale all light curves to common heliocentric and topocentric distance and correct all light curves to a common phase angle of 0°, as well as estimate Charon's flux and subtract it from each point.

In Tholen & Tedesco (1994, hereafter TT94), the Pluto-Charon B magnitude was modeled as a short Fourier series, including terms for the system's rotational light curve (which has an amplitude of roughly 30%), a secular dimming term, and a linear phase-angle term:

$$B(\alpha, \tau, \theta) = \sum_{n=0}^{4} (a_n \cos n\theta + b_n \sin n\theta) + \beta\alpha + \gamma\tau \ , \quad (1)$$

where B is the Johnson B magnitude at heliocentric and topocentric distances both equal to 1 AU, θ is the rotational phase, α is the phase angle, and τ is the Julian day relative to the reference epoch 2,444,240.66101.

All of the events used in this paper include a pre- or postevent segment. For each event, the offset between the average *observed* and *modeled* out-of-event baselines is subtracted from each point in the light curve (in magnitude space) to bring all of the observations to the photometric scale defined by TT94.

In addition to setting the events to a common reference level, we would like to remove Charon's contribution from the observed flux. Recent *Hubble Space Telescope* (*HST*) imaging at several rotational phases easily separates Pluto and Charon (Buie, Tholen, & Wasserman 1997a, hereafter BTW97). Similar to TT94, BTW97 use a short Fourier expansion to represent Pluto's and Charon's separate V magnitudes:

$$V(\alpha, \lambda) = \sum_{n=0}^{M} (a_n \cos n\lambda + b_n \sin n\lambda) + \beta\alpha \ , \quad (2)$$

where V is the Johnson V magnitude at heliocentric and geocentric distances of 39.5 and 38.5 AU, respectively, α is the phase angle, and λ is the sub-Earth longitude on Pluto. To convert V to B magnitudes, we use $B-V$ values of 0.868 and 0.710 for Pluto and Charon, respectively, where 0.868 is an intermediate value between the extremes of 0.873 and 0.863 (BTW97). We use both equations (1) and (2) (despite their similarity) because equation (1) describes the secular dimming of the Pluto-Charon system and equation (2) models the separate light curves of Pluto and Charon. Note that equation (2) uses east longitude as its argument, in contrast to equation (1), which uses rotational phase (which increases in the opposite direction).

To estimate Charon's flux at any instant, we first estimate the system's flux from the TT94 Fourier series. Then we estimate Charon's fractional flux [simply $C/(C + P)$, where C and P are Charon's and Pluto's individual fluxes based on the model of BTW97] and multiply it by the system flux to obtain Charon's contribution to the light curve.

In Figure 2, the resulting 18 light curves are plotted together to show that their baselines are roughly constant. The preevent baseline level of 0.8 is the result of converting

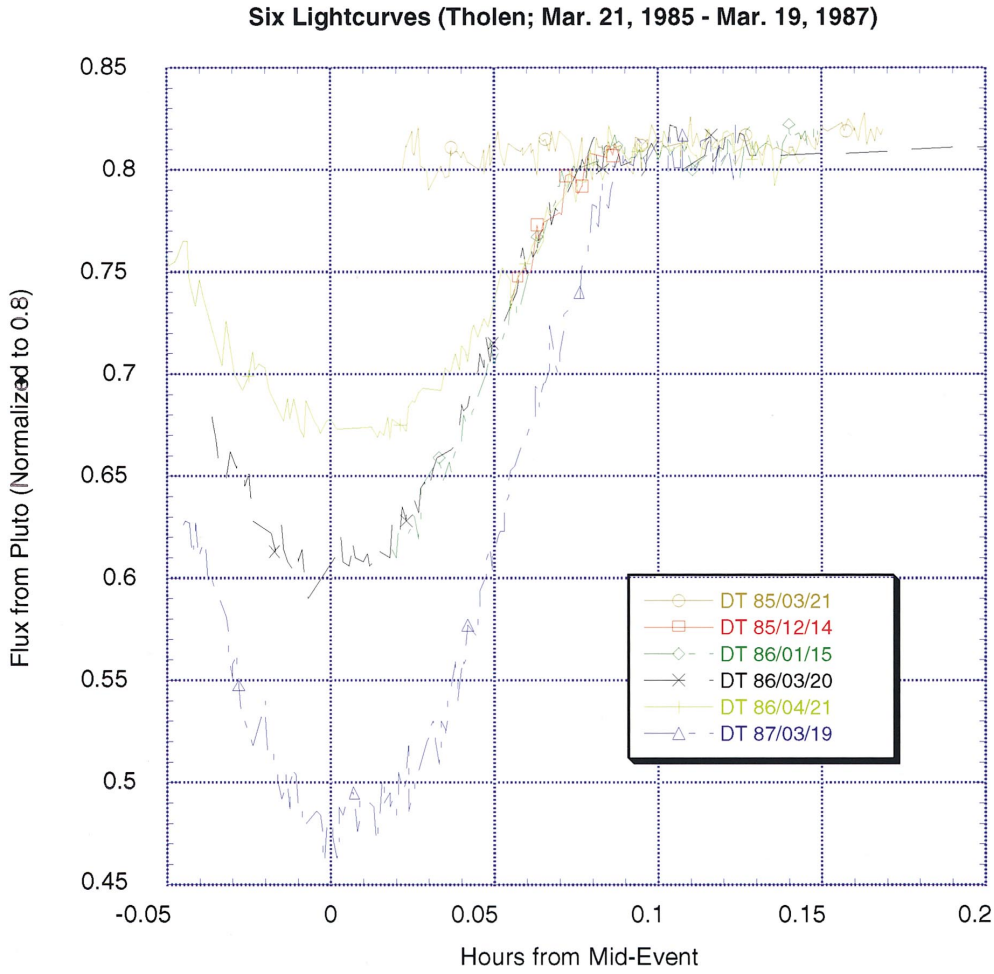

FIG. 2.—*Continued*

Pluto's magnitude at topocentric and heliocentric distances of 1 AU to fluxes relative to a zero-magnitude object.

3. THE LINEAR LIGHT-CURVE INVERSION PROBLEM

3.1. *Modeling the Flux from Pluto*

We divide Pluto into a grid of 48 latitude and longitude elements ranging from S90° to N90° and W97°.5 to E97°.5 and model the flux from Pluto as the sum of fluxes from all of the resulting surface elements. Note that the sub-Charon longitude on Pluto is defined as 0°, and the 7°.5 east and west of the nominal limb are sufficient to span any longitudes of Pluto that rotate into view during any of the 18 mutual events in this data set. Each pixel spans 3°.75 in latitude and 4°.06 in longitude, although polar pixels obviously have smaller areas than equatorial ones. The Earth-directed flux from a surface element is a function of its area, the angle its surface normal makes with the line of sight to Earth and the Sun, and (most obviously) whether the surface element is covered by Charon or its shadow. The exposed, projected, illuminated area of a surface element is

$$da = R_p^2 \cos\delta\, d\delta\, d\lambda(\hat{\boldsymbol{n}}\cdot\hat{\boldsymbol{e}})(\hat{\boldsymbol{n}}\cdot\hat{\boldsymbol{s}})(\text{exposure flag})\,, \qquad (3)$$

where da is the exposed, projected, illuminated area of a surface element, $d\delta$ and $d\lambda$ are infinitesimal latitudes and longitudes, respectively, $\hat{\boldsymbol{n}}$ is the surface normal unit vector for an area element, $\hat{\boldsymbol{e}}$ is the unit vector pointing from the surface element to Earth, $\hat{\boldsymbol{s}}$ is the unit vector pointing from the surface element to the Sun, and the *exposure flag* is a mask with a value between 0 and 1, depending on what fraction of the surface element is exposed or covered by Charon's disk or shadow.

Each surface element will have a normal reflectance, which is an unknown parameter to be determined in a least-squares fit. At any instant the modeled brightness of Pluto is the sum of the fluxes from all of the surface elements. The flux from any element is da times its normal reflectance. In other words, the observed light curves are approximated by a linear combination of surface element reflectances,

$$\boldsymbol{D} \approx \mathbf{F}\boldsymbol{x}\,, \qquad (4)$$

where $\boldsymbol{D}$ is the data vector, $\boldsymbol{x}$ is the vector of unknown reflectances, and $\boldsymbol{F}$ is the transformation matrix that relates the two. We seek a solution for $\boldsymbol{x}$ by trying to minimize the residuals

$$\boldsymbol{R} \approx \boldsymbol{D} - \mathbf{F}\boldsymbol{x} \qquad (5)$$

(we are using the convention that vectors in data space are capitals [such as $\boldsymbol{R}$ and $\boldsymbol{D}$], and vectors in model space [e.g., $\boldsymbol{x}$] are lowercase). The rows of matrix $\mathbf{F}$ are the exposed, projected areas for all of the surface elements. Each row determines the instantaneous coefficients for the elements of $\boldsymbol{x}$ so that they add up to an estimate of a single light-curve point.

There are circumstances in which this linear model is inadequate. If, for example, the apparent normal reflectance

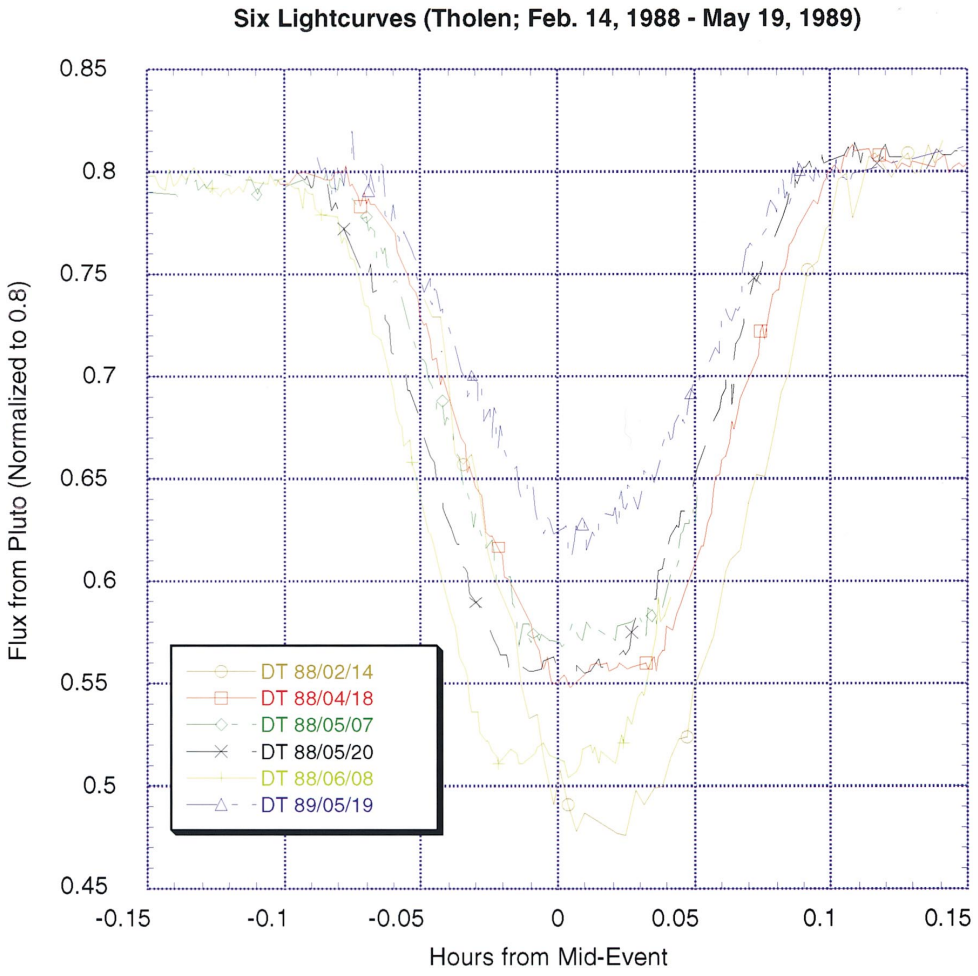

FIG. 2.—*Continued*

of a surface element were a strong function of the angles of incidence and emission, it would make sense to choose model parameters that are more intrinsic properties of the surface, such as single-scattering albedos and Hapke scattering parameters. Since this paper is based solely on mutual-event light curves, our viewing geometry is very restricted. We are taking snapshots of Pluto's sub-Charon hemisphere; even the earliest and latest out-of-event observations are only 2.5 hr before or after midevent (a small fraction of Pluto's 6.4 day period). Therefore, we present maps that are a *combination* of surface brightness and scattering effects. Our mutual-event coverage spans such a small range of rotations (less than $\pm 6°$) that we do not attempt to fit for separate scattering and surface brightness parameters.

3.2. *Adjoint versus Inversion*

3.2.1. *Problems with Least-Squares Inversion*

The brute-force method of determining $\mathbf{x}$ is to invert $\mathbf{F}$ (or $\mathbf{F}^T\mathbf{F}$) and find the "answer" in a single iteration. That solution would almost certainly contain unphysical albedos: negative normal reflectances (very rare in nature) and reflectances much greater than 1. The reason the inverse is noise sensitive stems from the fact that the surface brightnesses are determined from point-to-point differences in the light curve. Each time Charon moves a small distance over Pluto's disk, the normal reflectance of a small, banana-shaped region is determined from the difference between two consecutive points in the light curve. If a noise spike causes the second of two consecutive points to be higher than the first, *even though Charon actually covers more area at the second time step*, then the incremental part of Pluto's disk that is covered between the two time steps would be best fitted by a negative reflectance. A more robust scheme is to iteratively apply the *adjoint* of $\mathbf{F}$.

3.2.2. *The Adjoint versus the Inverse*

We use repeated applications of the adjoint as an alternative to the inverse. A lucid description of this technique, plus numerous geophysical examples, is contained in Jon Claerbout's book Geophysical Estimation by Example (Claerbout 1998).[1] This section is drawn directly from Claerbout's chapters 1 and 2.

The word "adjoint" has different meanings in different fields; in this context we mean the "conjugate transpose" of a matrix or linear operator. Since the $\mathbf{F}$-matrix is real, its adjoint *is* its transpose.

How could the transpose of $\mathbf{F}$ possibly yield a solution in place of its inverse? If a matrix is orthonormal, its conjugate transpose *is* the inverse. Our $\mathbf{F}$-matrix is not likely to be orthonormal, but repeated applications of the adjoint $\mathbf{F}^T$ are superior to inversion. Claerbout discusses this point in chapter 1:

[1] This book has the added advantage of being available on-line from http://sepwww.stanford.edu/sep/prof.

Our usual task is to find the inverse of these calculations; i.e., to find models (or make maps) from the data. Logically, the adjoint is the first step and part of all subsequent steps in this **inversion** process. Surprisingly, in practice the adjoint operator sometimes does a better job than the inverse! This is because the adjoint operator tolerates imperfections in the data and does not demand that the data provide full information....

When the adjoint operator is *not* an adequate approximation to the inverse, then you apply the techniques of fitting and optimization explained in Chapter 2. These techniques require iterative use of the modeling operator and its adjoint.

The adjoint operator is sometimes called the "**back projection**" operator because information propagated in one direction (earth to data) is projected backward (data to earth model).

How does one apply the adjoint?

1. Determine residuals: $\boldsymbol{R} \approx \boldsymbol{D} - \mathbf{F}\boldsymbol{x}$.
2. Transform residuals into the gradient: $\boldsymbol{g} = \mathbf{F}^T\boldsymbol{R}$.
3. Apply steepest descent (slow): take a step in the $\boldsymbol{g}$-direction; or
4. Apply conjugate directions (better): take a step in a direction that is a linear combination of $\boldsymbol{g}$ and the previous step.
5. Return to step 1.

Understand that step 2 is not going to arrive at the minimum in one iteration. The adjoint acts mainly on the most egregious mismatches in the residuals vector. The largest elements of the residuals vector are transformed (by the adjoint) into the dominant elements of the gradient vector. The updates to $\boldsymbol{x}$ are determined from a step along the gradient (combined with the previous step's direction). Ten iterations are sufficient to generate a map that is remarkably similar to earlier mutual-event mapping efforts (Fig. 3).

If we continue beyond 25 iterations, does the map improve? Yes, from the standpoint of reducing residuals, but emphatically not from the goal of making a credible map. A property of the conjugate directions algorithm is that it will converge to the inverse after N iterations, where N is the number of data points. After approximately 25 iterations, the conjugate directions algorithm starts to fit the noise in the light curves, having already fitted the resolvable albedo features. Beyond $\sim$25 iterations, we see many illegal reflectances in the solutions, meaning values that are negative or in excess of 1 (Fig. 4).

3.3. *Additional Constraints: Bounding the Light Curves*

An effective way of preventing illegal reflectances in the solution is to use the light-curve differences to constrain the solution. What albedo distribution corresponds to the greatest possible drop between two consecutive observations? When any just-covered (or less illuminated) regions are bright and any just-exposed (or more illuminated) regions are dark. Conversely, the greatest increase in flux between two light-curve points occurs when the just-covered areas are dark and the just-exposed areas

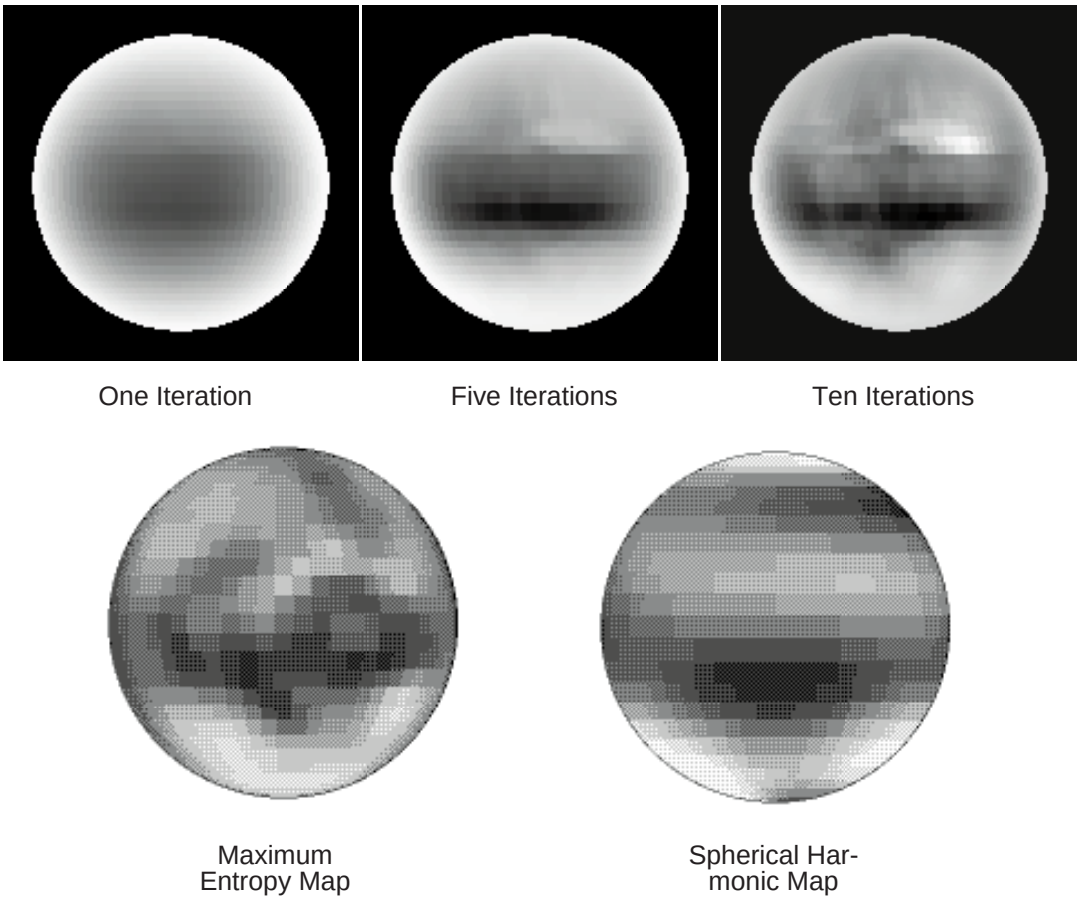

FIG. 3.—Comparison of conjugate direction maps (one, 10, and 25 iterations) with the maximum entropy map and spherical harmonic map

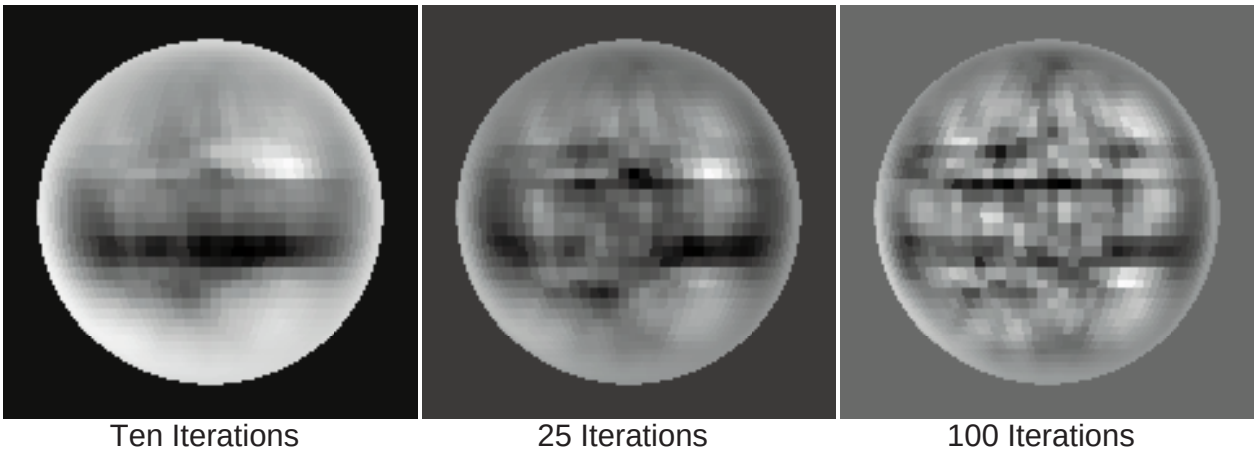

FIG. 4.—Maps after 10, 25, and 100 iterations. These maps have been autoscaled, but the brightest and darkest elements in the 100-iteration map have reflectances ranging from close to 1.8 down to nearly −1.

are bright. Areas on Pluto change their exposure and illumination either by rotating closer to or farther from the sub-Earth and subsolar points or by being covered or uncovered by Charon.

1. Suppose the just-exposed areas happen to be very bright and the just-covered areas are very dark. This case corresponds to an *upper bound* on the difference between the $(N + 1)$th point and the Nth point. Any greater difference between the $(N + 1)$th and Nth points would require albedos that are impossibly bright or impossibly dark (i.e., negative).

2. Alternatively, if we assume that the just-exposed areas happen to be very dark and all the just-covered areas are very bright, then we have a *lower bound* on the difference.

We know the exposed areas from time step to time step, and we can put limits on plausible values for "very bright" and "very dark" (1 and 0 for starters), so we can calculate an envelope that must bound legal differences. Since a complete light curve looks something like a U, the differences should look like the derivative of a U, which is something like a sideways S (Fig. 5).

Derivative space is particularly useful for illustrating differences in the light curves that *cannot possibly* correspond

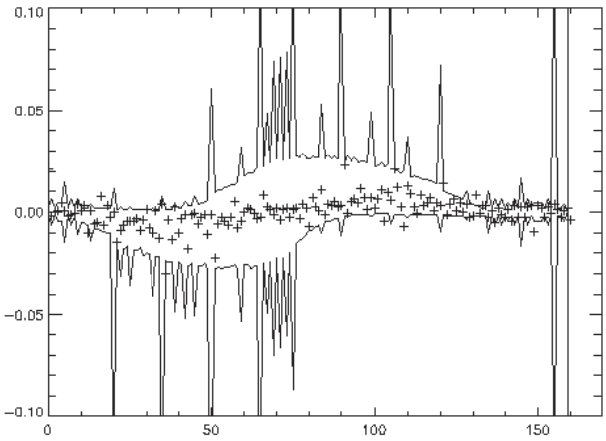

FIG. 5.—An envelope overlaid with differences. The spikes represent large steps in time between successive observations, with a poor constraint on the difference being the result. The light-curve differences that fall outside the envelope cannot be explained by legal surface albedo distributions.

to any legitimate surface reflectance distribution. We decided to apply constraints in derivative space to ensure that the reflectance solutions lie between "very bright" and "very dark." We now describe how we incorporated the derivative constraints in the conjugate directions algorithm.

The first step in the conjugate directions algorithm is building a vector of residuals. The residuals vector becomes the gradient vector (pointing the way to a better solution) through a transformation by the adjoint. Ordinarily, the residuals vector is the difference between the observed light curves and the model light curves. We constructed a second residuals vector from the "out of bounds" information of the light curves' differences. Elements of the new residuals vector are zero unless a particular difference between two successive observations is outside of the derivative envelope, in which case the residual is set to the amount by which the difference is out of bounds. We concatenate this second residuals vector to the first one, and we append a matrix $\mathbf{F}_{\text{dif}}$ to the matrix $\mathbf{F}$ (see eq. [7]). $\mathbf{F}_{\text{dif}}$ is very closely related to $\mathbf{F}$; since $\mathbf{F}_{\text{dif}}$ creates the forward differences of the light-curves vector $\boldsymbol{D}$, $\mathbf{F}_{\text{dif}}$ is equal to $\mathbf{F}$ minus a version of $\mathbf{F}$ whose rows have been cycled upward by one time step:

$$\begin{aligned}\boldsymbol{\Delta} = \boldsymbol{D} - \boldsymbol{D}_{\text{shifted}} &= \begin{pmatrix} D_1 \\ D_2 \\ D_3 \\ \vdots \end{pmatrix} - \begin{pmatrix} D_2 \\ D_3 \\ D_4 \\ \vdots \end{pmatrix} \\ &= \mathbf{F}\boldsymbol{x} - \mathbf{F}_{\text{shifted}}\boldsymbol{x} \\ &= \left[\begin{pmatrix} F_{11} & F_{12} & F_{13} & \cdots \\ F_{21} & F_{22} & F_{23} & \cdots \\ F_{31} & F_{32} & F_{33} & \cdots \\ \vdots & \vdots & \vdots & \ddots \end{pmatrix} \right. \\ &\quad \left. - \begin{pmatrix} F_{21} & F_{22} & F_{23} & \cdots \\ F_{31} & F_{32} & F_{33} & \cdots \\ F_{41} & F_{42} & F_{43} & \cdots \\ \vdots & \vdots & \vdots & \ddots \end{pmatrix} \right] \boldsymbol{x} = \mathbf{F}_{\text{dif}}\boldsymbol{x}\,, \end{aligned} \tag{6}$$

where $\boldsymbol{\Delta}$ is the vector containing the differences between each light-curve point and its predecessor. Our old linear equation was $\boldsymbol{D} \approx \mathbf{F}\boldsymbol{x}$. Our new version—including the con-

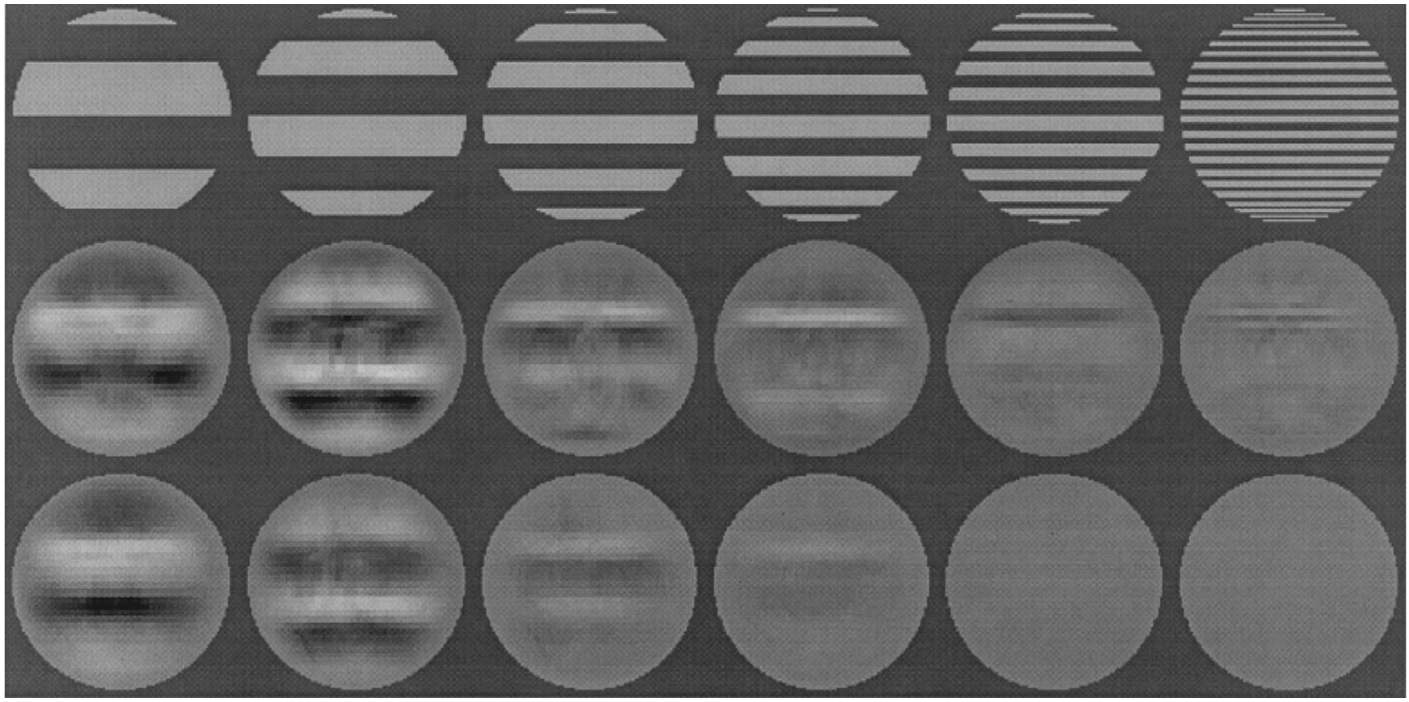

FIG. 6*a*

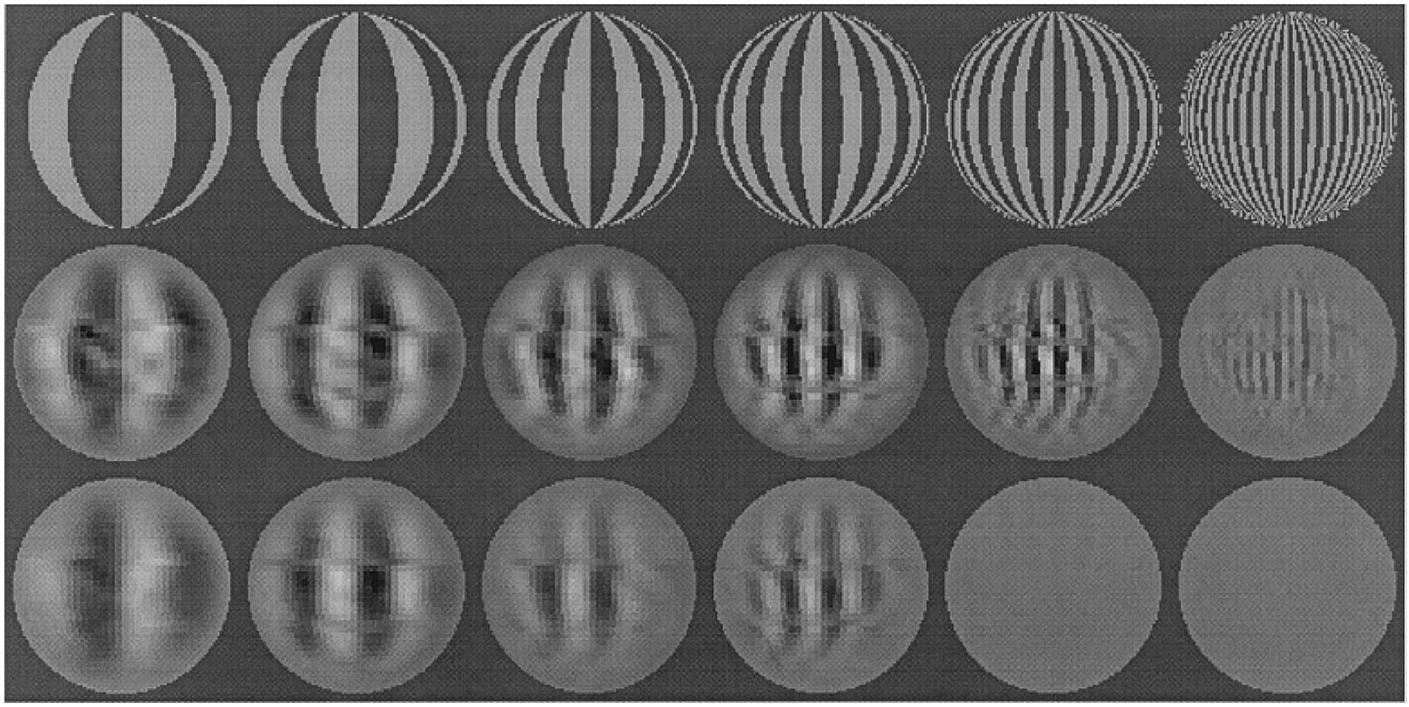

FIG. 6*b*

FIG. 6.—(*a*) Latitudinal spatial resolution test. *Top*, the "original" Plutos; *middle*, reconstructions from noise-free light curves without constraints on the point-to-point differences; *bottom*, reconstructions from noisy light curves with constraints on the light-curve differences. (*b*) Same as (*a*), but for the longitudinal spatial resolution test.

straints on the differences—is

$$\begin{pmatrix} \boldsymbol{D} \\ \boldsymbol{\Delta} \end{pmatrix} \approx \begin{pmatrix} \mathbf{F} \\ \mathbf{F}_{\rm dif} \end{pmatrix} \boldsymbol{x} \, . \tag{7}$$

The difference-bounding constraints are successful on several fronts:

1. The map solutions no longer have any illegal reflectances.

2. The fit *with* the constraints converges much faster than the fit *without* the constraints. ("Converge" is defined by no change to the double-precision value of the reduced χ^2, the sum of squared residuals per degree of freedom. Convergence typically takes around 50 iterations.)

3. Although the fit with the constraints has a larger χ^2 than the fit without, the constraints on the differences have a minimal impact on the solution, given that they guarantee legal reflectances. Other schemes (smoothing, low-pass fil-

tering, or constraining the reflectances themselves) might have a higher impact on the solution, resulting in a greater loss of spatial resolution. One can change the impact of the second residuals vector by multiplying it (and $\mathbf{F}_{\rm dif}$) by a weighting factor (essentially a Lagrangian multiplier). We have used a weighting factor of 1, but it is straightforward to trade off spatial resolution with constrained albedos.

What is the best weighting factor to use? Larger weighting factors prevent illegal solutions at the expense of fitting the observed light curves. Our weighting factor of 1 is large enough to prevent negative albedos, but small enough to smooth the map only slightly. We have generated map solutions using a few Lagrangian multipliers to confirm that larger weighting factors smooth the map, and smaller ones allow illegal albedos, although we have not exhaustively searched smaller multipliers.

3.4. *Spatial Resolution Tests*

To test the ability of this data set and map-making procedure to resolve surface features on Pluto, we constructed a series of synthetic Plutos. We generated synthetic light curves from these test Plutos to mimic the original observations, adding Gaussian noise scaled by each point's original estimated error. We had expected the resolution in longitude to be better than the resolution in latitude, since every light curve contains tens or hundreds of points that subdivide Pluto's disk in longitude but there are only 18 separate cuts across Pluto's disk in latitude. For this reason we built separate synthetic Plutos to test latitudinal and longitudinal resolution (Figs. 6*a*, 6*b*).

Figure 6 illustrates several important points. For example, even the simulations with no added noise (*middle rows*) cannot reproduce all of the original Pluto. Pluto's limb is not resolved, and the skinniest line patterns (3°.75 per line) are not resolved, particularly in the latitude test. Adding the bounding constraint on the light-curve differences (*bottom rows*) does degrade the spatial resolution (compare the bottom rows with the middle rows). On the other hand, the solutions with constraints (*bottom rows*) are legal. Noisy reconstructions *without* constraints on the differences (not shown) produced reflectances ranging from -0.8 to 1.7.

The tests with the bounding constraints show that the resolved regions are limited to a central disk that is roughly 45° in radius. Does this mean that the poles cannot be resolved, even though the 1985 February and the 1990 February events transited Pluto's north and south poles, respectively? Not exactly—we would have to shift the test pattern in Figure 6*a* up and down by small increments to completely characterize the mutual events as a "transfer function" for Pluto's albedo distribution. There are bound to be certain vertical phase shifts for which the latitudinal test pattern in Figure 6*a* can be well resolved over the poles, namely, phase shifts corresponding to the width of the paths that Charon cut across the north pole in 1985 February and the south in 1990 February.

We have only reconstructed these 12 test patterns (six latitudinal, six longitudinal) shown in the top rows of Figures 6*a* and 6*b* to show the spatial resolution in the central region of Pluto's disk. The bottom rows of Figure 6 show that we can resolve 11°.25 bands in longitude and 15° bands in latitude. These correspond to roughly 235 and 314 km, respectively, in the center of Pluto's disk.

4. RESULTS

4.1. *The Map*

The map shown in Figure 7 is a fit to the combined set of 18 light curves (a grand total of 1977 points) of D. J. T. and R. P. B. With constraints on the differences between consecutive points, the fit converges between 45 and 50 iterations.

Salient features of the map include the following:

1. Even with the poor spatial resolution at the poles, it is clear that the south pole (A) is brighter than the north pole. While the north pole *may* have bright frost deposits that this map fails to resolve, the south pole certainly does have bright frost deposits. The south-north dichotomy of Pluto's sub-Charon hemisphere shown in this map repeats the findings of Buie et al. (1992) and Young & Binzel (1993).
2. There are some very dark regions on Pluto. In particular, there is a patch (B) at S15°, E19°, roughly 500 km in longitude by 300 km in latitude, with normal reflectances less than 0.1. There is also a dark wedge (C) at W7° extending southward into the bright polar region from about S30°.
3. The most noticeable feature is a bright area (D) at N17°, E33°. This isolated patch is roughly 250 km in diameter.
4. The map shows a dark patch (E) at N17° on the meridian, less than 200 km in diameter. This patch lies at the same latitude as the bright patch at E33°. Clearly, the bright patch at N17° is a different phenomenon from the bright latitudinal "equatorial collar" found on Triton by *Voyager*.

We have binned Pluto's surface elements by surface brightness, since that information is expected to be relevant to models of frost transport or spectral models of surface composition (e.g., Cruikshank et al. 1997). Figure 8 tabulates the percentage of *disk-projected* surface units that have normal reflectances between 0 and 0.1, 0.1 and 0.2, etc. We use the projected areas of surface elements because that is what observers see when they image or take spectra of Pluto.

Is this map unique, or is there another reflectance distribution that could produce an equally low value of χ^2? The model is linear, which means we have found the global χ^2 minimum. On the other hand, any details in the map that are smaller than the nominal resolutions indicated in Figures 6*a* and 6*b* are not significant. In fact, the number of grid elements (2304 elements; 48×48 elements) exceeds the number of light-curve points (1977 total). The adjoint method is quite happy to work on such an undetermined problem; it simply corrects the regions of the map that are responsible for the largest contributions to the residuals. We have made maps with grid resolutions of 32×32 and 56×56; both of those cases converge to solutions that are nearly identical to the 48×48 grid we present here, except that they look respectively coarser or finer.

It is worth pointing out that the additional constraints on the light-curve differences do not ensure a unique solution, although they certainly help. In fact, if the observational noise were completely benign (i.e., no illegal albedos necessary to fit the light curves), then the light-curve difference constraints would not actually constrain the solution at all. One could use other constraints to achieve a unique solution, such as maximizing the entropy of the map. In the meantime, keep in mind that some pixels are highly correlated with their neighbors, especially in regions that are

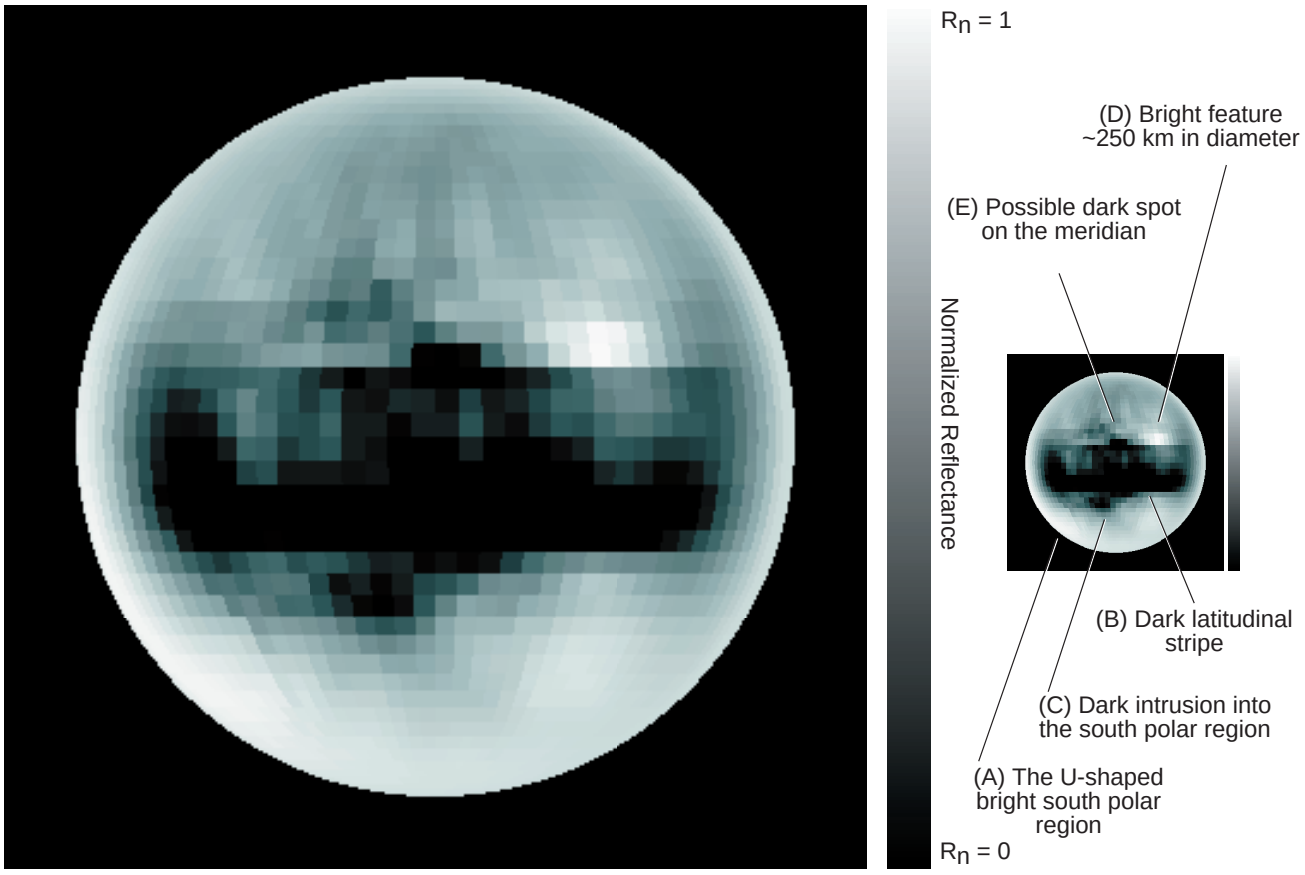

FIG. 7.—*B*-filter map of normal reflectances of Pluto's sub-Charon hemisphere. Units are normal reflectances.

poorly resolved (like the limb and poles), and while the total flux reflected from a resolved region is a robust quantity, the smaller pixel-to-pixel variations are not.

4.2. *Error Estimates*

We estimate the errors by generating many map solutions with different normally distributed random noise added to the original light curves for each run. The element-by-element errors shown here (Fig. 9) are the rms values of the solutions from 20 separate runs. With one exception, all of the rms errors are less than ± 0.1. Why are the errors lower over the poles than at the disk center, given that many more events transited the center? Our adjoint solution resolved the disk center into far smaller resolution elements than at the poles or limb. The errors over the poles and limb represent errors for much larger areas than at the disk center.

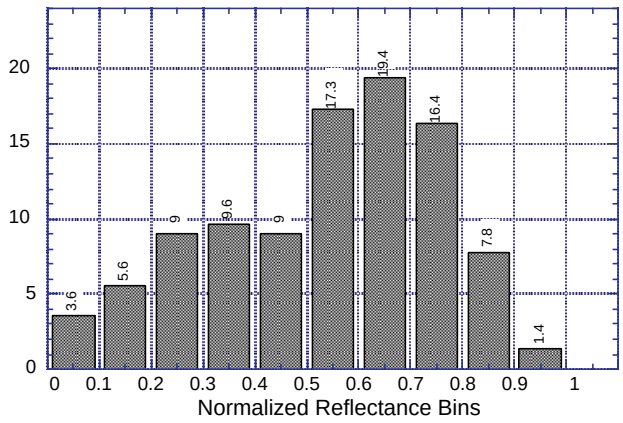

FIG. 8.—Histogram showing the percentage of disk-projected areas that fall into 0.1 bins of normal reflectance.

Another concern is the photometric processing, which *must* be consistent across all events. The two signs that an individual event is too bright or too dark are stripes across Pluto's disk corresponding to the edges of the transit event and a broad dip or rise in the residuals vector. The latter is probably easier to detect. Figures 10*a* and 10*b* show an example in which one light curve (from 1988 May 7) is augmented by a constant offset of 5% of its preevent baseline value.

The bright feature (D) is suspect, given the relatively high error over one of its pixels. Could this bright spot be caused by a few bad light-curve points? We tested that hypothesis by generating a residuals vector from a map in which the bright spot was darkened to a normal reflectance of 0.5. The difference between these new residuals and the unaltered-map residuals tells us exactly which light-curve points affect the map solution over the bright feature. It turns out that 269 observations (out of 1977 total) constrain the albedo of feature D, and these 269 points are spread out over 10 separate events. We therefore believe that feature D is not an artifact.

4.3. *Comparison with HST FOC Map*

Pluto has been imaged directly by the *HST* Faint Object

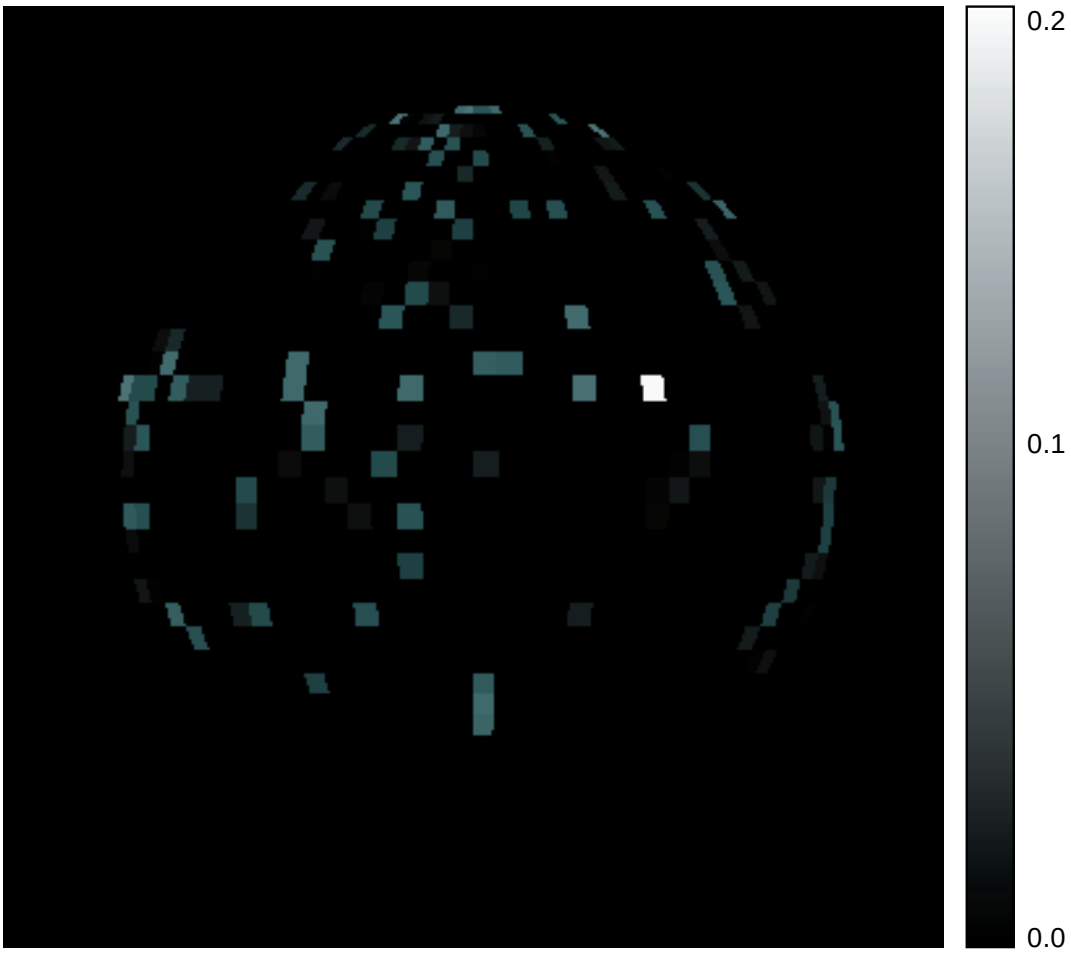

FIG. 9.—Error map. Note that the errors are universally below ± 0.1, except for one pixel with an rms error of ± 0.22.

Camera (FOC) (Stern, Buie, & Trafton 1997) in wavelengths similar to the Johnson *B* filters used in R. P. B.'s and D. J. T.'s mutual-event light curves. Figure 11 compares the *HST* map with a smoothed version of the map shown in Figure 7, both from the perspective of the sub-Charon hemisphere. The smoothed mutual-event map was convolved with a Gaussian kernel with an FWHM of 16°.

Pluto's subsolar latitude is moving north at a rate of approximately 2° yr^{-1}. The mutual events cover the period from 1985 through 1990, but the *HST* images were taken in 1994. The subsolar latitude crossed the equator in 1989; since that time, Pluto's south pole has (1) moved increasingly into permanent shadow and (2) grown foreshortened to earthbound observers. Both effects make it extremely difficult for the *HST* images to resolve the south pole. Nevertheless, the bright southern feature is large enough to be detected by the *HST* map. Furthermore, both the *HST* and the mutual-event maps show a dark incursion into the bright southern feature just to the west of the sub-Charon longitude (i.e., just left of center). Both maps show a dark region across the middle of the disk, on the northern edge of the southern bright feature. The bright feature at N17° in the mutual-event map is smeared into a larger bright region in the north that roughly coincides with a similar feature in *HST* map, but the *HST* map has another bright feature in the north near the central longitude of the disk, in conflict with the dark region in that area in the smoothed mutual-event map.

5. DISCUSSION

5.1. *Implications of the Map*

In agreement with earlier mutual-event maps, we find a bright southern cap on Pluto's sub-Charon hemisphere extending as far north as S30°. This bright frost feature is still a mystery, given that the entire southern hemisphere was in constant sunlight for 124 years prior to 1989 (Binzel 1990). Our map improves the resolution of the bright southern region's boundary, which is clearly not a simple latitudinal boundary. Typical reflectances for the bright southern cap range from 0.75 to 0.91.

We also find no evidence of a similarly bright region originating from the north pole, although our resolution is not good enough to preclude bright frost deposits ~ 100 km in diameter or less at the higher northern latitudes. Typical reflectances above N45° are generally 0.59–0.72, slightly higher than the disk average of 0.52.

The darkest large region on the disk is a band at roughly S12°. The latitudinal structure of this feature made us suspect that it was an artifact due to a photometric error in one or more of the light curves. We experimented with maps in which events that transited that latitude were omitted, and the dark band persisted. On that basis we conclude that the dark band is a real feature.

What could cause this dark band at S12°? One possibility is that the contrast between the dark band and the bright southern regions is maintained by a feedback effect. The

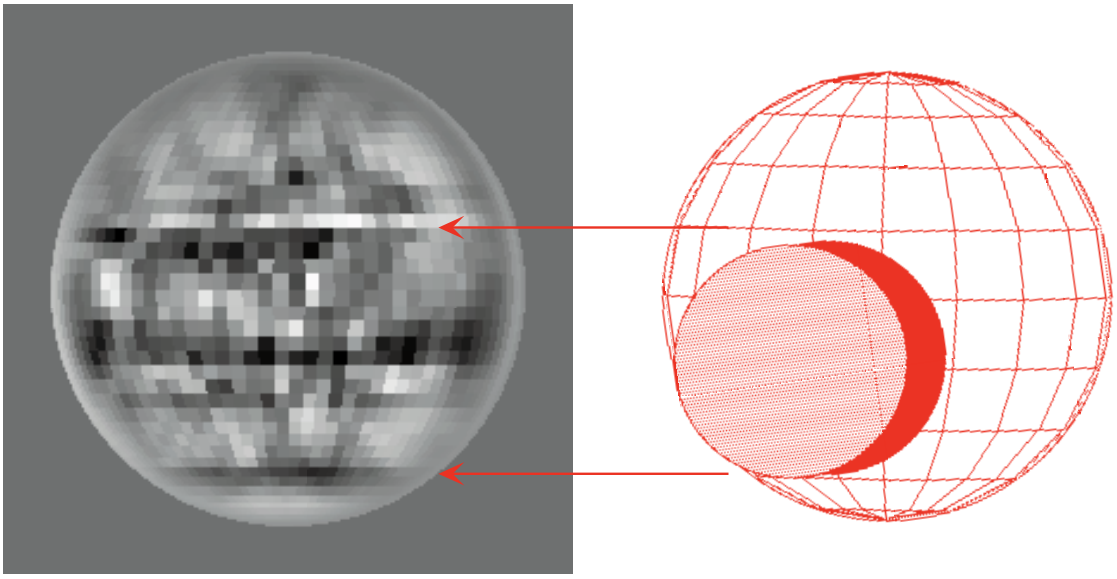

FIG. 10*a*

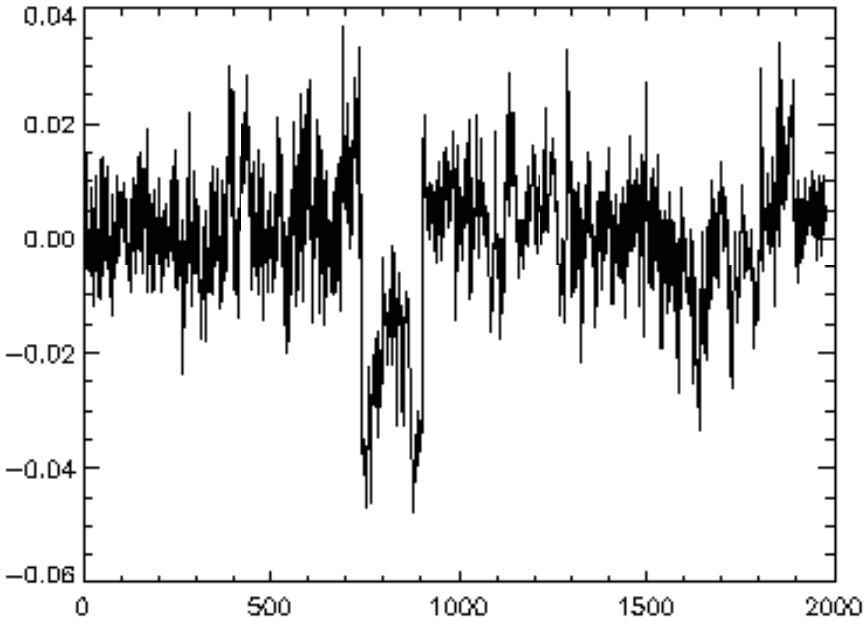

FIG. 10*b*

FIG. 10.—(*a*) Testing the effects of errors in photometry. Here the 1988 May 7 event has been increased by 5% of its nominal baseline level. Bright and dark "racing stripes" are visible at the edges of the transit event. (*b*) A better indicator of bad photometry is the residuals vector, which clearly shows that the entire May 7 event is too bright (and hence the residuals vector, $\mathbf{F}x - \boldsymbol{D}$ in this case, is too low over that event).

bright southern regions reflect most of the incident sunlight, and as a result they stay cool and remain condensation sites, even if they receive more incident sunlight than the neighboring dark band. Presumably, the warmer, darker band would become still darker as volatiles sublimated from that region, leaving lag deposits to darken the frost.

The isolated bright feature at N17° has an extremely high normal reflectance of 0.95. We offer several speculative suggestions for what this feature might be:

Condensation around a "geyser."—Plumes were seen on Triton, and condensates around volcanos on Io affect the surface reflectances.

A terrain effect.—Could the bright feature be a large crater, for example? For that matter, would condensation occur on elevated or sunken terrain on Pluto?

Condensation can occur when a volatile's vapor pressure is less than the actual pressure (supersaturation can also occur, obviously). Consider the following cases:

1. Pluto's temperature profile near the surface follows a dry adiabat. Given Pluto's N_2 atmosphere, the temperature would increase by ~ 0.6 K for every kilometer lost in elevation:

$$\frac{dT}{dz} = \frac{-g}{c_p} \approx \frac{0.64 \text{ m s}^{-2}}{1004 \text{ J}} . \tag{8}$$

In this case a crater would *not* be a condensation site. The vapor pressure of N_2 is a steep function of temperature

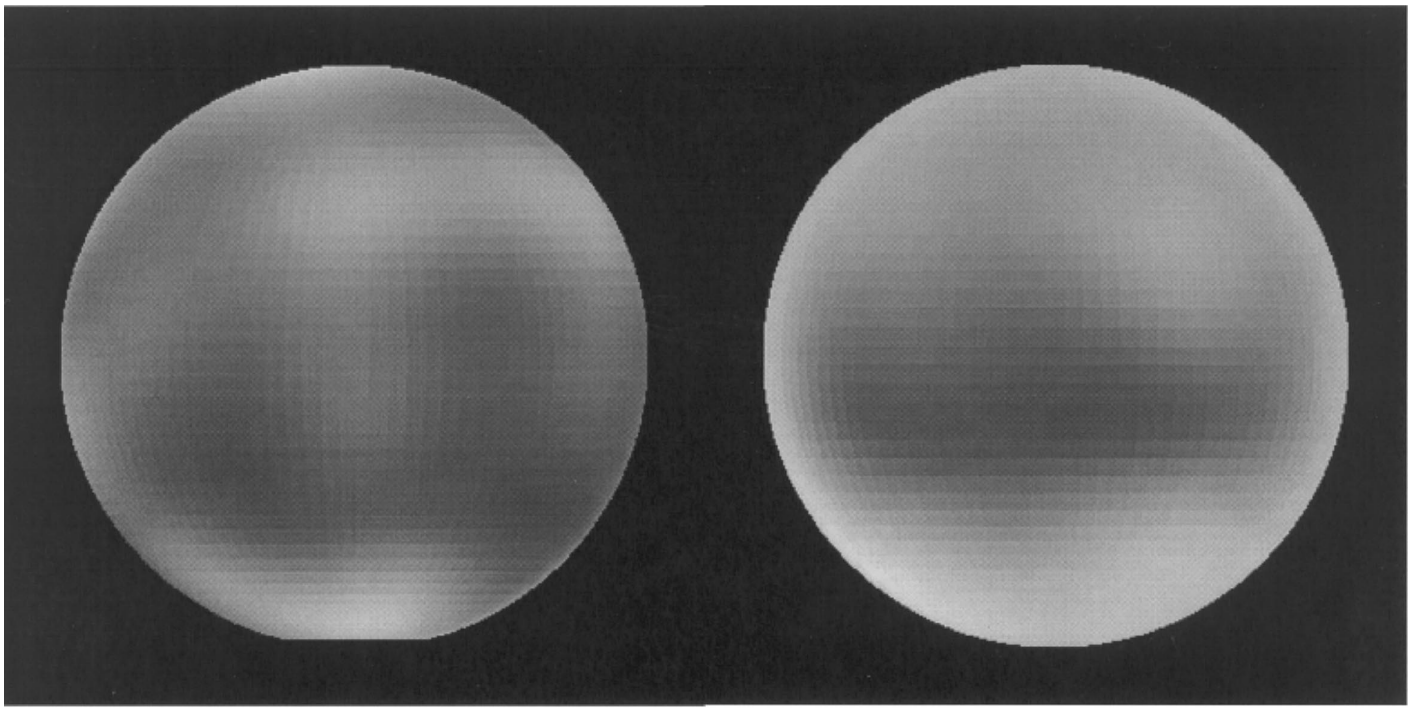

FIG. 11.—*HST* FOC map showing the sub-Charon face of Pluto (*left*) compared with a smoothed version of the mutual-event map shown in Fig. 7

(Brown & Zeigler 1980), enough so that the vapor pressure increases with depth more rapidly than does the surface pressure. To calculate the surface pressure, we have assumed a scale height of 29.8 km (Elliot & Young 1992) and a nominal surface pressure that is equal to 58 mbar, the vapor pressure of N_2 at $\sim$40 K (Tryka et al. 1994).

2. If the atmosphere is clear and thin, the surface temperature should be primarily a function of the Bond albedo of the surface itself. Consider two adjacent terrains, one high, one low, but with the same albedo. The vapor pressure is the same over both surfaces (because the temperatures are the same), but the actual pressure is greater over the lower site. Volatiles should therefore condense more rapidly on the lower site, at least until the frost buildup changes the surface temperature.

Appealing to Triton for insight is not much help in this case. There are dark wind streaks over Triton's south pole, suggesting that the plumes of Triton do not brighten a local area. Most craters on Triton seem to have the same albedo as their surroundings, although Mangwe Cavus does have a bright interior.

5.2. *Summary*

We have introduced a mapping technique that had not been applied to the Pluto-Charon mutual events. Combined with constraints on the light-curve differences, the use of the adjoint instead of the inverse results in higher spatial resolution and less sensitivity to noise. Reconstructions of test Plutos show that we can recover features as small as $\sim$235 km in longitude and $\sim$314 km in latitude. In comparison, previous mutual-event maps and the *HST* FOC maps can resolve features $\sim$450–500 km across (although *HST* has the advantage of being able to image *all* faces of Pluto, not just the sub-Charon hemisphere).

Our new map confirms the existence of an extensive bright southern feature, with normal reflectances above 0.75. This feature extends to S30° across most of Pluto's sub-Charon face, but its border is *not* a simple latitudinal limit. There is a dark wedge at around W15°–W30° that extends roughly 15° into the southern bright region. We find several local dark regions with normal reflectances less than 0.1. One in particular (at S12°) is notable in that it borders an area with normal reflectances close to 1. Since that bright area is undoubtedly a product of frost deposition, some explanation is needed as to why the adjacent area is not frost-covered as well.

We also find an isolated bright region at N17°, $\sim$250 km in diameter. With a reflectance over 0.95, this feature is also frost-covered. This feature raises a question: what could cause frost deposition over such a local area?

We still have no evidence for a northern frost cap to rival the southern one, at least over the sub-Charon face of Pluto.

5.3. *Possibilities for Future Work*

What is the dark material?—The dark areas are likely to be colored with CH_4 and N_2 photolysis by-products (Bohn et al. 1994). It would be interesting to make a map in wavelengths corresponding to CH_4 absorption bands to map the distribution of CH_4 or photolysis by-products with similar C—H stretch bands.

What are the temperatures of different surface units?—It may be that dark areas are devoid of volatiles and are not cooled by sublimation. Alternatively, some dark regions may be composed of CH_4 frost, as opposed to N_2 frost. These areas may reach temperatures higher than the 40 K frost temperature that Tryka et al. (1994) fitted to the N_2 frost spectrum, because CH_4 requires higher temperatures to reach the same vapor pressure as N_2. Such reservoirs of concentrated, warm CH_4 could explain the apparent over-

abundance of CH_4 in Pluto's atmosphere (Young et al. 1997). One useful project that is only marginally beyond current instrumentation is to acquire a rotationally resolved temperature light curve of Pluto.

What are the ages of different frost units?—On Triton, there is a suggestive correlation between frost that looks old (over Triton's southern hemisphere), which is relatively red, and frost that looks new (the "equatorial collar"), which is relatively blue. We plan to build a $B-V$ color map of Pluto based on mutual-event light curves obtained by R. P. B. The goal is to see if color units correspond to bright or dark units, or whether some frost features are bluer or redder than others.

REFERENCES

Andersson, L. E. 1978, BAAS, 10, 586
Binzel, R. P. 1990, BAAS, 22, 1128
Binzel, R. P., & Hubbard, W. B. 1997, in Pluto and Charon, ed. S. A. Stern & D. J. Tholen (Tucson: Univ. Arizona Press), 85
Binzel, R. P., Tholen, D. J., Tedesco, E. F., Buratti, B. J., & Nelson, R. M. 1985, Science, 228, 1193
Bohn, R. B., Sandford, S. A., Allamandola, L. J., & Cruikshank, D. P. 1994, Icarus, 111, 151
Brown, G. N., & Zeigler, W. T. 1980, Adv. Cryogenic Eng., 25, 662
Buie, M. W., Tholen, D. J., & Horne, K. 1992, Icarus, 97, 211
Buie, M. W., Tholen, D. J., & Wasserman, L. H. 1997a, Icarus, 125, 233 (BTW97)
Buie, M. W., Young, E. F., & Binzel, R. P. 1997b, in Pluto and Charon, ed. S. A. Stern & D. J. Tholen (Tucson: Univ. Arizona Press), 269
Claerbout, J. F. 1998, Geophysical Estimation by Example (Stanford, CA: Stanford Exploration Project)
Cruikshank, D. P., Roush, T. L., Moore, J. M., Sykes, M., Owen, T. C., Bartholomew, M. J., Brown, R. H., & Tryka, K. A. 1997, in Pluto and Charon, ed. S. A. Stern & D. J. Tholen (Tucson: Univ. Arizona Press), 221
Elliot, J. L., & Young, L. A. 1992, AJ, 103, 991
Stern, S. A., Buie, M. W., & Trafton, L. M. 1997, AJ, 113, 827
Tholen, D. J., & Tedesco, E. F. 1994, Icarus, 108, 200 (TT94)
Tryka, K. A., Brown, R. H., Cruikshank, D. P., Owen, T. C., Geballe, T. R., & de Bergh, C. 1994, Icarus, 112, 513
Young, E. F., & Binzel, R. P. 1993, Icarus, 102, 134
———. 1994, Icarus, 108, 219
Young, L. A., Elliot, J. L., Tokunaga, A., de Bergh, C., & Owen, T. 1997, Icarus, 127, 258